The International Journal of Advanced Manufacturing Technology (2020) 111:2405–2418
https://doi.org/10.1007/s00170-020-06210-z

ORIGINAL ARTICLE

Microstructural evaluation of WC and steel dissimilar bilayered composite obtained by spark plasma sintering

Mahadi Hasan[1,2,3] · Zhenyi Huang[1] · Jingwei Zhao[3,4] · Al Jumlat[3] · Fanghui Jia[3] · Hui Wu[3] · Zhengyi Jiang[3]

Received: 14 May 2020 / Accepted: 2 October 2020 / Published online: 13 October 2020
© Springer-Verlag London Ltd., part of Springer Nature 2020

Abstract

Spark plasma sintering (SPS) is a powerful technique for consolidating metal powders at a remarkably shorter time with excellent quality. We used this technique for sintering nanocrystalline WC10Co powders and simultaneously bonding with high-strength steel. A series of experiments were conducted in order to find out the optimised set of SPS controlling parameters. The effects of temperatures (1000 to 1150 °C, with a 50 °C interval) in sintering nanocrystalline WC10Co powders and their bonding phenomena with AISI4340 steel were examined at a constant pressure of 80 MPa and a holding time of 5 min. The full density of the carbide powders was achieved at a lower temperature compared with that of conventional techniques. A number of techniques were employed to evaluate the microstructural characteristics of WC and steel bilayered composite and their mechanical properties. For determining the bonding strength of the joint, a novel micro-tensile testing system was adopted. Since such investigation is the first of its kind, to the best knowledge of the authors, where SPS is used to join the tungsten carbide with the steel, this research is expected to provide a valuable future reference for fabricating dissimilar bilayered composite materials.

Keywords Spark plasma sintering · Layered composite · Micro-tensile test · Sintering parameters

✉ Zhengyi Jiang
jiang@uow.edu.au

Mahadi Hasan
mh001@uowmail.edu.au

Zhenyi Huang
huangzhenyi@ahut.edu.cn

Jingwei Zhao
jzhao@tyut.edu.cn

Al Jumlat
aja458@uowmail.edu.au

[1] School of Materials Science and Engineering, Anhui University of Technology, Maanshan 243002, China

[2] Department of Textile Engineering, Bangladesh University of Business and Technology, Dhaka 1216, Bangladesh

[3] School of Mechanical, Materials, Mechatronic and Biomedical Engineering, University of Wollongong, Wollongong, NSW 2522, Australia

[4] College of Mechanical and Vehicle Engineering, Taiyuan University of Technology, Taiyuan 030024, China

1 Introduction

Spark plasma sintering (SPS) is a popular and potential technique for consolidating metal and ceramic powders. The key benefits of SPS include rapid sintering capability, achievement of full density at a considerably low temperature and an excellent control over the grain sizes. As SPS involves a quick joule heating technique with applied pressure, it is not necessary to achieve eutectic temperature, particularly, when the ultrafine or nanocrystalline powders are used. This indicates that the powders used can achieve full density without rendering liquid state condition. It is worth mentioning that when controlling the temperature in SPS, usually there is a temperature gradient involved inside the sample and the graphite die depending on the design of the die materials; this range is from 30 to 300 °C [1]. Rapid heating and small holding time in SPS make it possible to control the sintering process and grain growth.

According to previous studies, high density of WC–Co can be achieved using the SPS technique, between 1050 and 1100 °C, by applying even medium pressure, e.g. 30–50 MPa. Cha et al.

[2] investigated the sintering of nanocrystalline WC10Co powders at 1100 °C and mentioned that the sintering occurred in a liquid state. Sivaprahasam et al. [3] used nanocrystalline WC12Co at the same temperature (1100 °C); however, they stated that the sintering of WC occurs in solid phase whereas the cobalt (binder materials) in WC grains acts like liquid phase sintering [3]. Huang et al. [4] studied the consolidating of WC–Co at 1100 °C and reported it to be a solid-state sintering. In order to measure the temperature gradient, they also used an empirical technique and found it to be ~ 150 °C. Thus, the ultimate temperature inside the samples (1100 + 150 °C) reached below the eutectic temperature (~ 1320 °C) of the Co-W-C system. Though this indicates that the consolidation at 1100 °C, most probably, occurred in solid phase, however, there was some similar morphological appearance in the WC grains that resemblances liquid phase sintering (i.e. from spherical to faceted grain structures) [4]. The temperature distribution incurred by SPS inside the WC–Co was also demonstrated by Liu et al. [5]. They stated that Co layers on the WC grains experience higher temperature, and thus, localised WC–Co contact zones may reach the eutectic temperature. This indicates that even at lower sintering temperature, there can be a thin layer of liquid phase presenting on the grain boundaries which may assist densification process [5]. Thus, the difficulties to attribute the densification behaviours (liquid or a solid phase) explain clearly the challenges to measure the temperature in SPS technique. Nevertheless, some indications could be given by analysing the microstructures. The solid-phase sintering of WC–Co provides some inhomogeneity in the microstructure, depending on some factors between WC and cobalt particles. For example, when WC particle size is smaller than Co, the inhomogeneity increases. On the other hand, it is important to mention that solid-phase sintering results in smaller grain size distribution and thus improves the mechanical properties [6, 7].

On the other hand, bonding between WC and steel is challenging because of their large difference in physical properties e.g. coefficient of thermal expansion [8, 9]. A number of different techniques have been reported in the past to bond WC and steel. Zafar et al. [10] inspected the bonding of WC-12Co with AISI 304 stainless steel, using a microwave hybrid heating technique. Feng et al. [11] researched the diffusion bonding of WC–Co/Ni and stainless steel and obtained a tensile strength of 195 MPa at 950 °C. Thomazic et al. [12] employed powder metallurgy to combine cemented carbides and steel. They also examined the effects of various parameters such as composition, compaction pressure, heating rate, sintering temperature and duration. Similar research was also performed by Pascal et al. [13]. Another common technique of bonding WC and steel is using an interlayer. A wide range of interlayer materials are used, including Cu/Ag-based solders [11]; multilayer brazing of Cu and Ni alloys [14–16]; interlayer coatings of CrN, ZrN and TiCxN1-x [17]; Ti interlayer [18] and electroplated Cu/Ni interlayer [19]. Haghshenas et al. [20] used the diffusion brazing of AISI 4145 steel to WC–Co cemented carbide using RBCuZn-D interlayer with bonding temperature values of 930, 960, 990 and 1020 °C. The main reason for employing an interlayer is to alleviate the mismatch of the coefficient of thermal expansion (CTE) of these two materials. Another popular technique of depositing WC on steel material is high-velocity oxy-fuel (HVOF). Nascimento et al. used WC and successfully sprayed on AISI4340 through HVOF [21]. Monticelli et al. used WC-12Co on carbon steel [22]. Similar investigations were also performed in [23–25]. Though HVOF is a pragmatic technique to deposit WC on steel, however, it is a coating technique and thus only a limited thickness can be achieved on the steel surface. Recently, a novel technique called hot compaction diffusion bonding (HCDB) was employed to bond WC and steel. A Gleeble 3500 thermal-mechanical simulator was used for hot pressing and sintering. In HCDB, a diffusion-based powder-solid bonding mechanism was employed and a successful bonding was achieved between WC and steel [26, 27]. These researches provide fundamental knowledge on the effects of various experimental parameters, bonding mechanics and microstructure analysis. Nevertheless, studies on bonding between WC and steel are still a flimsy. Better manufacturing technique, attaining stable and stronger bonding, further microstructural characterisation and mechanical property evaluation are still the scopes of investigation.

In this study, the sintering behaviour of nanocrystalline WC10Co of 100-nm particle size was examined. In addition, their bonding phenomena with AISI4340 were also examined. The effects of sintering temperature ranging from 1000 to 1150 °C with a 50 °C interval and SPS controlling parameters were analysed. A constant pressure of 80 MPa was employed with a sintering time of 5 min. The sintering quality of WC10Co powders and their bonding phenomena with AISI4340 steel were analysed. A number of characterisation techniques, including optical microscopy, scanning electron microscopy equipped with Aztec energy-dispersive spectroscopy and backscattered electron, X-ray diffraction and electron backscatter diffraction, were employed. The mechanical properties were evaluated by examining microhardness, density measurement and micro-tensile strength tests. For determining the tensile strength of the joint, a novel microsystem was adopted as reported in [28]. Since this is the first study of its kind, to the best knowledge of the authors, where SPS is used to join WC10Co powders and solid AISI4340, it is expected that this research can provide valuable reference for joining ceramic and steel materials to manufacture dissimilar bilayered functionally graded composite materials. Such materials could potentially be used in the applications where both high hardness and high strength are necessary.

2 Experimental

SPS, also familiar as field assistant sintering technique, is a sintering scheme that uses high-pulsed DC current at very low voltage for heating. In this system, the sample powders are placed inside a die, usually made of graphite and acts as a heating component when the current is passed through it. The Joule effect is used to heat up the die. In this case, the powders are conductive, and the current also passes through the sample, experiencing some additional heating internally. Consequently, a uniaxial compression pressure is applied in order to minimise the requirement of sintering temperature and holding time. Figure 1 presents the schematic diagram showing the working principle of the SPS system. The experiment is conducted in a vacuum environment of $2.0X10^{-2}$ Torr. A thermocouple is usually used to regulate the sintering process, inserted through a hole from the bottom spacer. Sometimes, pyrometers are used; however, in that case, the readings at lower temperature are not that accurate. For the detailed working procedures of SPS [1–6], studies could also be referred.

Commercially available, near-spherical shaped plasma arc discharged nanocrystalline WC10Co powders with an average particle size (APS) of 100 nm and AISI4340 rod of 12 mm diameter were used in this study. SEM micrographs of the used powders and their chemical compositions are mentioned in our previous work [20].

Figure 2 shows the photograph and dimension of the AISI4340 used in this study which was purchased from Bohler Uddeholm, Australia, with a dimension of 12 mm diameter and 8 mm height. Table 1 presents the details of the experimental parameters used in this study. The sintering temperature varied from 1000 to 1150 °C with an interval of 50 °C. A constant pressure of 80 MPa and holding time of 5 min were applied. These parameters were chosen based on the literature [1–6] and experiments. Moreover, a number of experiments were unsuccessful in the beginning which were due to inappropriate controlling parameters involved in running the SPS machine. This includes heating rate, cooling rate and applying pressure rate, which play a significant role to successfully finish the experiment. As the information is rarely available in the literature, a number of trial and error experiments were needed to perform, for the successful completion of the experiments.

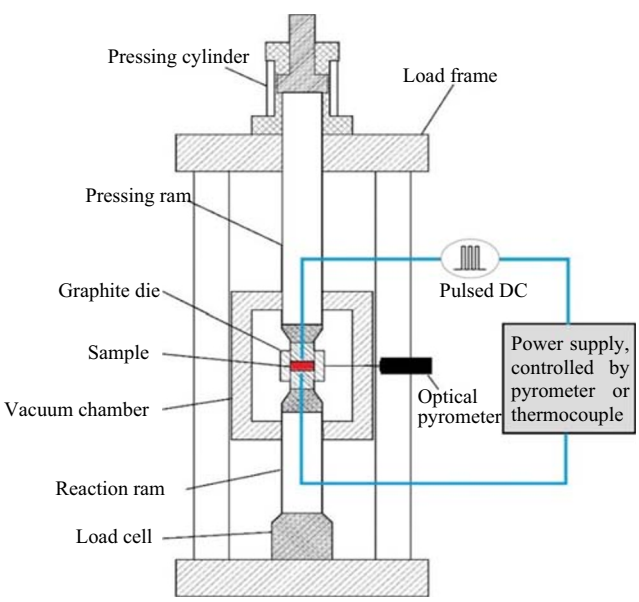

Fig. 1 Schematic diagram representing the working principle of the SPS machine

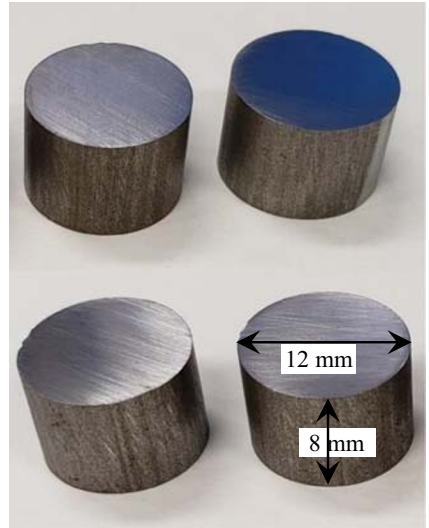

Fig. 2 Photographs and dimensions of AISI4340

For examining the microstructure of the sintered carbides and their bonding quality with the steel, the specimens were cut along the cross-section. Fanuc Robocut α-OiD hig-precision wire cutting with 0.25-mm-diameter wire was used to cut the samples. Specimens for measuring the tensile strength of the bond were also prepared by wire cutting. A 3D illustration as shown in Fig. 3 presents the sequence of sample cutting mechanism. After cutting, the specimens were mounted in 20 ml of polyfast resin by CitoPress mounting press machine (Struers) followed by grinding and diamond polishing down to 0.25-μm and OP-S Chemical treatment. The microstructure was observed by JEOL NEOSCOPE SEM equipped with backscattered electron EDS. The distribution of chemical elements at the bonding interface was examined through built in EDS in NEOSCOPE SEM. The phases formed during the

Table 1 Experimental parameters used in this study

Parameters		Variables			
Temperature °C	Variables	1000	1050	1100	1150
	Fixed values	Pressure: 80 MPa, time: 5 min			

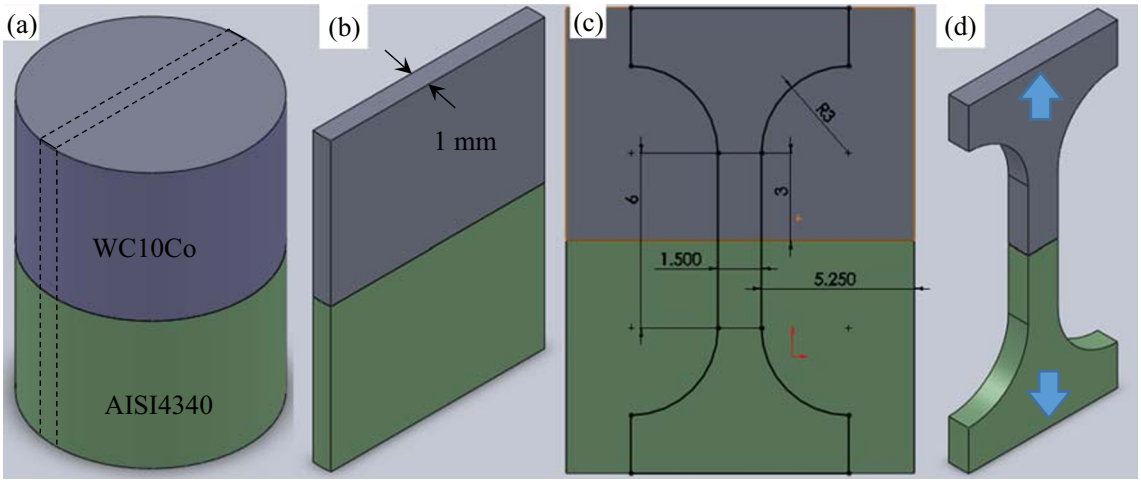

Fig. 3 Sequence of preparing tensile test specimen: **a** 3D diagram of the bilayered ceramic steel composite, **b** cut section from the middle part of the specimen using Fanuc Robocut α-OiD wire cutting machine, **c** dimensions for cutting the tensile test sample, and **d** 3D illustration of the final tensile test specimen

sintering process were identified by XRD using monochromatic Cu Kα radiation in GBC MMA diffractometer, with an angular step size of 0.05°, and a speed of 2°/m, at 35 kV and 28.4 mA. The mechanical properties were evaluated by examining the microhardness, density and direct tensile strength of the bond. The microhardness indentations were carried out across the sample, using a Matsuzawa Via-F automatic microhardness tester under 50-N load and dwell time of 10 s.

The bonding strength of the fabricated bilayered composite was determined by a miniature tensile test system. According to the best knowledge of the authors, such investigation to determine the direct tensile bonding strength of WC10Co and AISI4340 has not been reported in the past. By considering the size effects, the tensile test specimens were scaled down, and therefore, the thickness of each sample was only 1 mm. Consequently, a miniature system was employed as depicted in [28]. Figure 4 shows the setup used for the tensile test. Figure 5 presents a typical image of the prepared sample cut from the fabricated dissimilar bilayered composite. Since the specimen is small in size, conventional elongation measurement could not be used. Therefore, a non-contact elongation measuring system was employed. An image processing program was used in MATLAB to calculate the strain. A rectangular area was marked by contrasting colour on the middle of the sample. A microscope, as shown in Fig. 4, was used to capture the video focusing on the coloured area; the video was then separated into individual images using the MATLAB program. The images were then transferred to the grey level and then to binary images. During this transformation, a process for noise reduction was performed to eradicate the small areas where the colour was lost during the test. Thus, the errors caused by colour loss in the marked area can be avoided. As a result, boundaries on the marked area can be found by colour value comparison among adjacent pixels. If the colour value is zero or one for a particular pixel in the binary image, of which the neighbouring pixels are different, the pixel was selected as a boundary point. After all such boundary points are detected, the points were sorted according to their X and Y coordinates, sequentially. This leads to four groups of points on four boundaries of the coloured area. The displacement along the length direction can be calculated based on these boundaries. By comparing the length of the marked area, in each image, the strain can be acquired. Correspondingly, a force sensor was used to record the tensile force which was transferred to the computer. By matching the video and the force recording frequencies, both engineering and true stress-strain curves can be obtained.

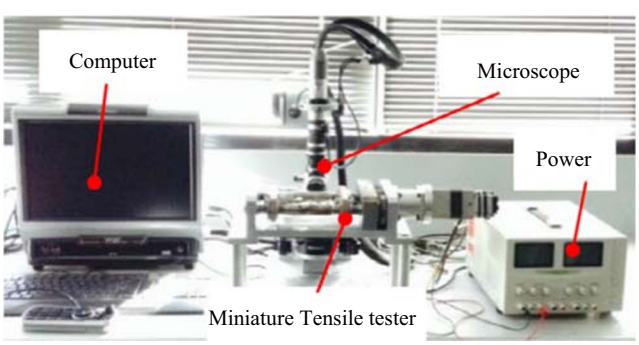

Fig. 4 Setup for miniature tensile test system [28]

3 Results and discussion

3.1 Microstructure

The microstructure of the WC10Co/AISI4340 bilayered composite fabricated by SPS was observed by SEM. The distribution of chemical elements on the interface was also investigated through elemental mapping using EDS. The effects of

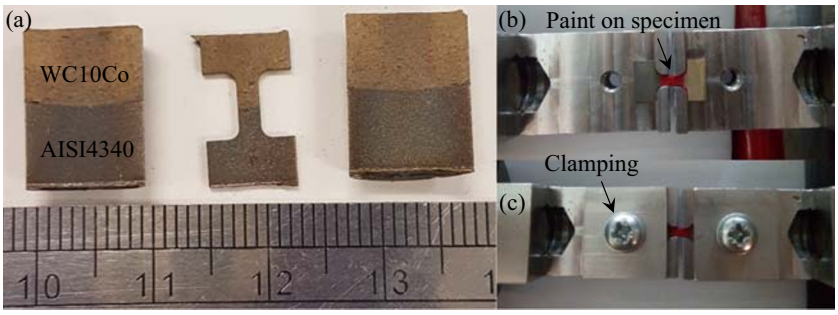

Fig. 5 Tensile test sample preparation, **a** prepared sample, **b** painted sample which is mounted on the miniature tensile tester, and **c** clamped sample ready for tensile testing

sintering temperature on the microstructure of the composite were examined. It is evident that in all experimental conditions, the bonding between the two materials takes place. No significant fracture or crack is observed, particularly at elevated temperature, indicating a successful bonding occurred under all conditions. Nevertheless, the quality of sintering and bonding mainly depends on the experimental conditions applied. Hence, as mentioned earlier, one of the main challenges in such novel experiments was to successfully complete the experiment. For smooth operation of the experiments, it was found that increasing pressure in the beginning and then slowly heating the samples, followed by an increased rate of applying pressure as well as rapid heating, result in successful completion of the experiments without exploding the powder particles or damaging the die-punch setup due to abnormal overheating. In addition, from the microstructure, it appears that the consolidation at all temperatures happened in solid phase which is analogous to the study conducted by Huang et al. [4]. Hence, the temperature gradient between the thermocouple and the samples placed inside the graphite die is estimated to be ~150 °C, which, in turn, specifies that the ultimate temperature inside the same is below the eutectic point of Co-W-C system. In addition, the smaller grain sizes as can be seen from the microstructures (Figs. 6b and 8d) and the improved mechanical properties of the sintered carbides (Figs. 10, 11, and 12) are the indications of solid-phase sintering as reported in [6.7].

Figure 6 shows the typical SEM image at the interface of WC10Co and AISI4340 bilayered composite, obtained at 1000 °C, sintered for 5 min under a pressure of 80 MPa. Figure 6a shows the overall microstructure in a large area of the bilayered composite with a low magnification image. Figure 6b presents closer view of the interface with high magnification. It can be noticed that microvoids exit in the carbide regions, indicating insufficient sintering because of inadequate temperature and sintering time. Due to these reasons, minor microcracks appeared at this low temperature. Apparently, the interface mostly exhibits a crack-free and continuous bonding between the ceramic and steel materials resulting in a successful bonding. From the microstructure (Fig. 6b), bonding between carbide and steel materials took place without any significant delamination. However, the quality of sintering is poor as can be seen by lots of voids/cavities. The corresponding EDS areal maps show the elemental distribution of the key elements (W, Fe, Co, C, O and Ni) in the bonding area. It is clearly seen that migration of the alloying elements took place, indicating successful bonding of WC10Co and AISI4340. However, this migration occurred on a limited scale which gives an indication that the bonding is not that strong at this stage.

Figure 7 presents the elemental spectrum and composition of the elements. The elemental spectrum was constructed on the region as shown in Fig. 6(b). The spectrum was obtained keeping the interface region in a place as middle as possible while capturing the spectrum. It confirms the presence of allowing elements with the highest peaks of tungsten and iron. The percentage of the compositions (in the middle of the image) also indicates a fair distribution of the elements in the sample.

With increasing sintering temperature, the sintering of the carbide powders as well as their bonding quality with the steel can significantly be improved. Figure 8 shows the SEM image of the composite obtained at 1150 °C, sintered for 5 min under the compaction pressure of 80 MPa. It is clearly seen that the sintering quality of the powders largely improved. Negligible amounts of micropores are present. The interface appears crack-free, indicating sound metallurgical bonding of the WC10Co and AISI4340. Figure 8a shows the consolidated area of WC10Co without any significant voids/cavities. However, one can notice that there are some sequentially increase of white regions towards the interface. The white regions present agglomerated carbide powders with slightly poor quality of sintering compared with that at the top regions. This indicates that the sintering quality near the punch area is somewhat better than the far area of the punch, i.e. near the interface. Figure 8b presents a larger view of the bonding area of WC10Co and AISI4340 with lower magnification. A crack-free, continuous and successful bonding is clearly observed. Figure 8 c and d show the magnified image of the bonding interface representing clear view of the microstructure. A tight mechanical contact between the two layers indicates stronger

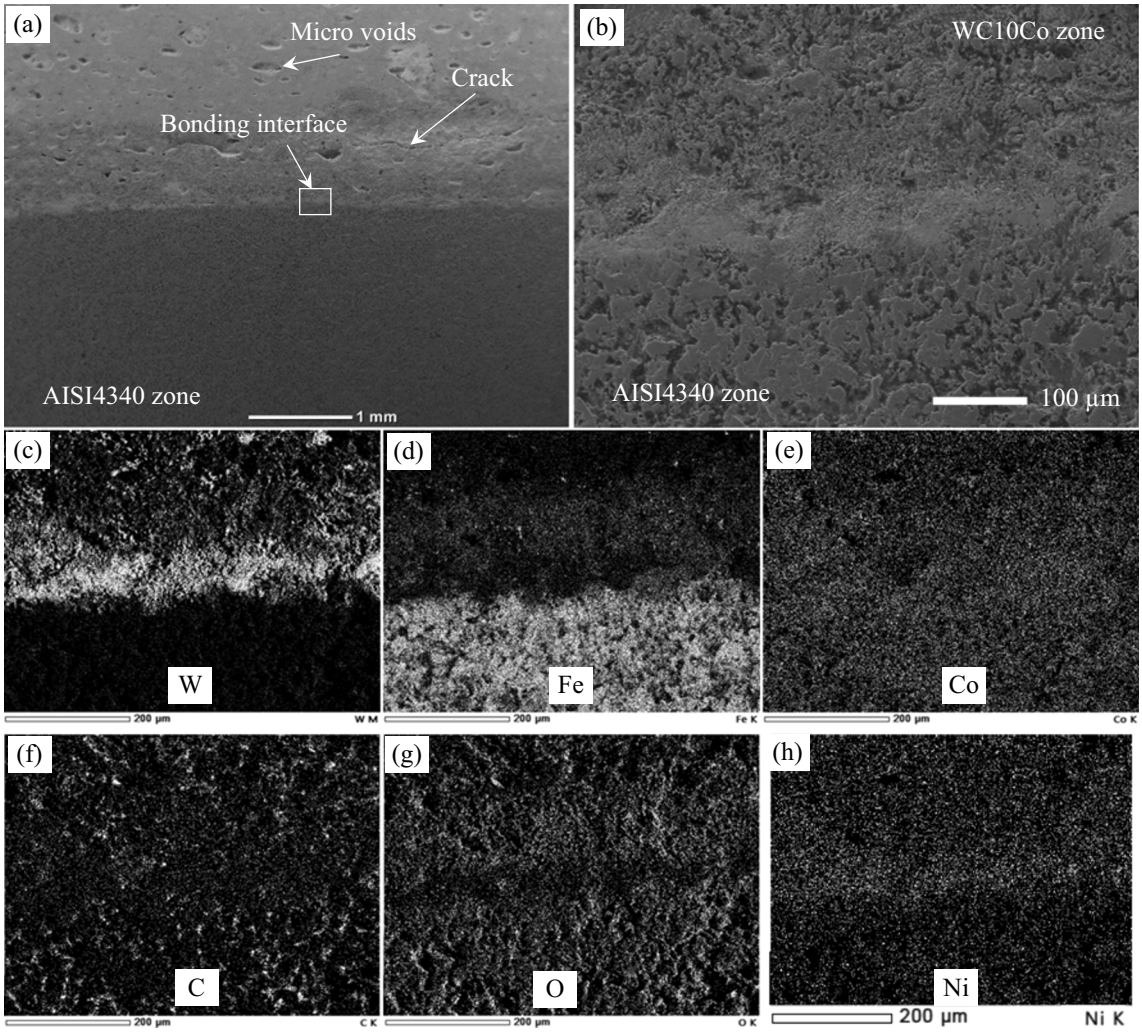

Fig. 6 Typical SEM images and EDS maps of the WC10Co and AISI4340 bilayered composite, **a** sintered at 1000 °C, for 5 min under 80-MPa pressure; **b** magnified view of **a** EDS maps showing **c** W, **d** Fe, **e** Co, **f** C, **g** O and **h** Ni elements

bonding to take place between WC10Co and AISI4340. The corresponding EDS areal maps show the elemental distribution of the key elements (W, Fe and Co) in the bonding area. It is clearly seen that the migration of the alloying elements took place, indicating successful bonding between WC10Co and AISI4340.

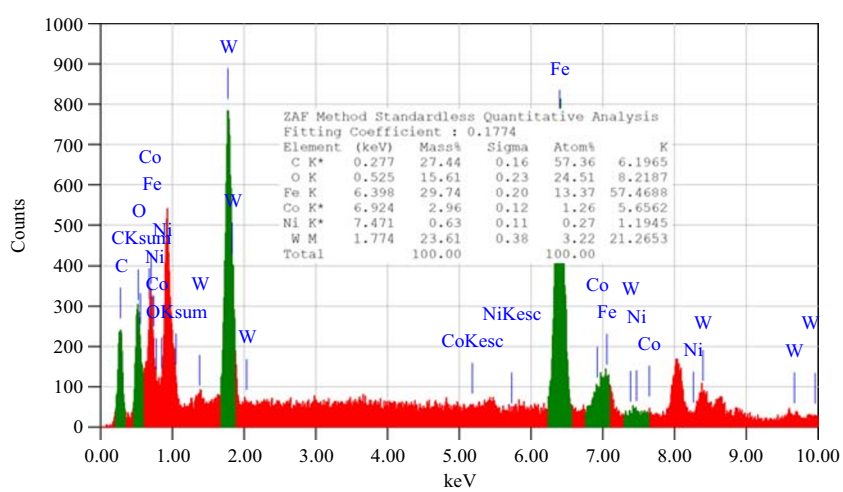

Fig. 7 Elemental spectrum showing the peaks of the elements

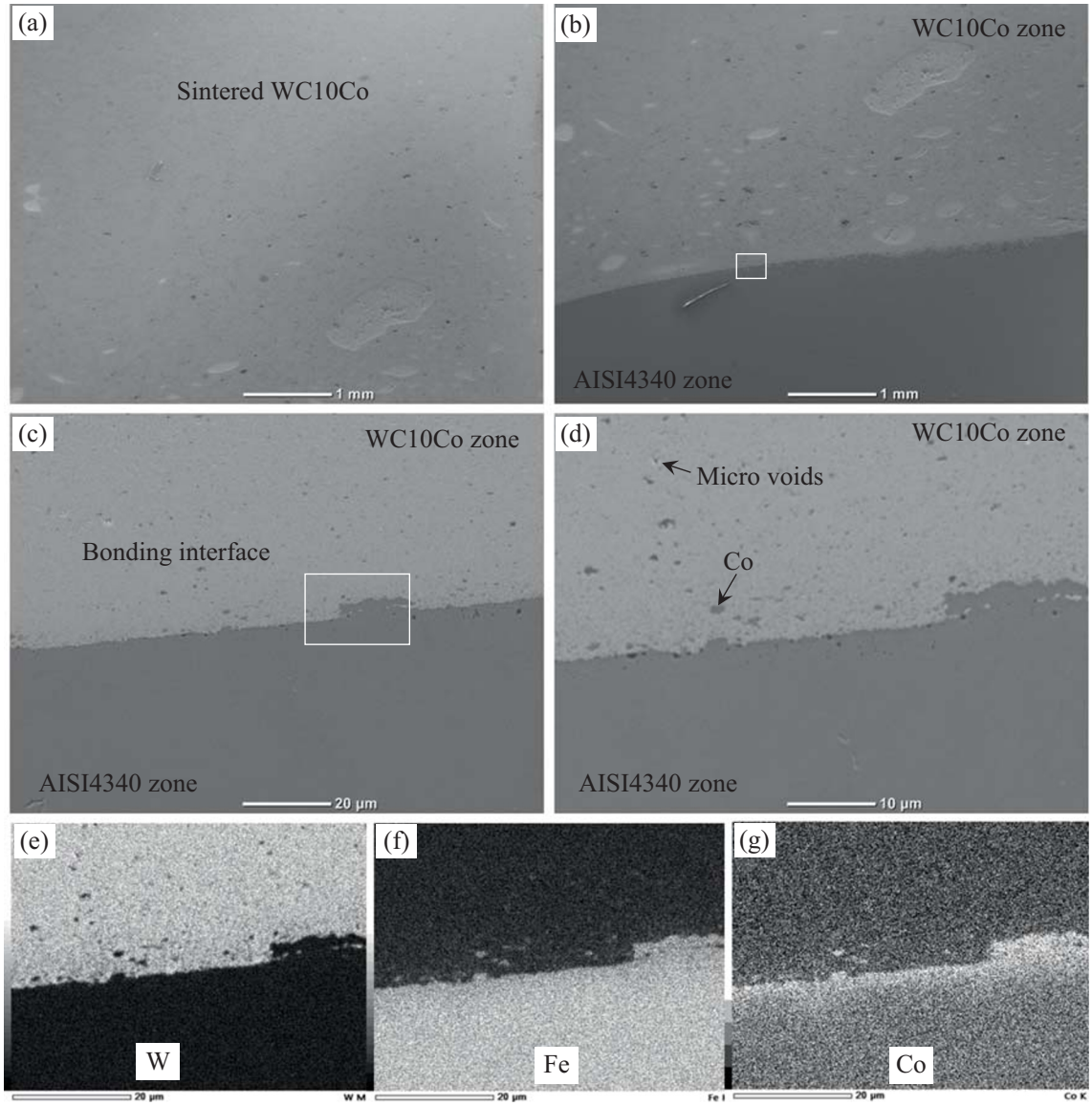

Fig. 8 Typical SEM images of the WC10Co and AISI4340 bilayered composite, sintered at 1150 °C, for 5 min under 80-MPa pressure, **a** consolidated WC10Co region, **b** bonding interface, **c** magnified view of the bonding interface, and **d** further magnified SEM image of the bonding interface and EDS maps showing **e** W, **f** Fe and **g** Co elements

3.2 Phase analysis

The XRD patterns of the WC10Co/AISI4340 bilayered composite were recorded using a GBC MMA diffractometer with an angular 2θ diffraction between 25 and 100°. Diffractograms were collected with an angular step size of 0.02° at 1°/m. Cu Kα radiation was obtained from a copper X-ray tube operated at 35 kV and 28.4 mA. The formed phases were identified using X'Pert High Score Plus.

The spectra of XRD are illustrated in Fig. 9. The influence of the change in temperature during sintering and bonding of WC10Co and AISI4340 by SPS is indicated. The details of the phases, including their chemical formula, ICCD card no and crystal structure information, are listed in Table 2. It is revealed that, at lower temperatures such as 1000 °C (Fig. 9), the phases are mainly composed of tungsten carbide (WC), iron (Fe) and iron cobalt (Fe_3Co). The formation of Fe_3Co superlattice phases is evidenced in the presence of Fe and Co above 550 °C [29, 30], with tetragonal crystal system and P4/mmm space group. The chemical reaction involved is as follows in Eq. 1 [30].

$$3Fe_3 + Co_3 = 3Fe_3Co \quad (1)$$

With the increase of temperature, along with WC, the other phases identified include iron manganese (FeMn), iron oxide (FeO), tungsten carbide (W2C) and traces of ternary phase such as tungsten iron carbide (W_6Fe_6C). FeMn is usually

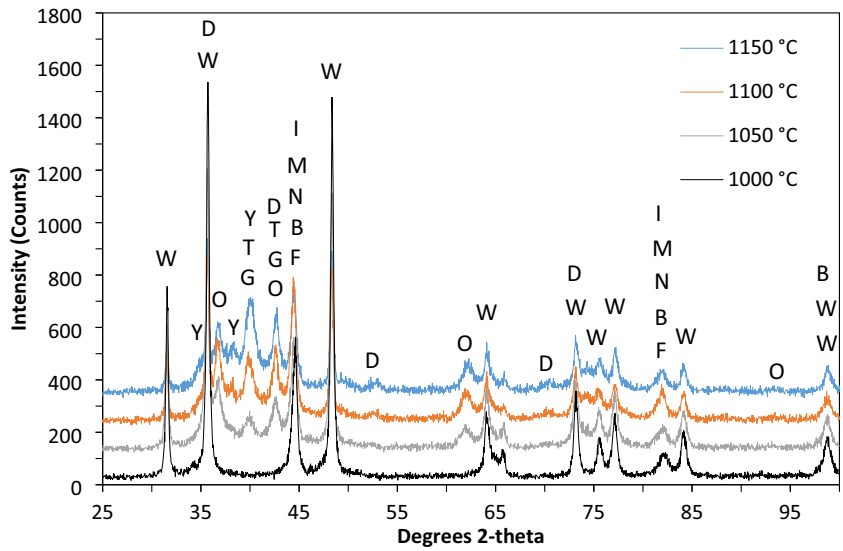

Fig. 9 XRD results showing the effects of temperature from 1000 to 1150 °C with a gap of 50 °C sintered for 5 min under 80-MPa uniaxial pressure

formed at above 1000 °C and the presence of which is confirmed by the XRD peaks as denoted by M (Fig. 9). Likewise, FeO is formed under high temperature and pressure condition as reported in [31]. The decomposition of WC and formation of W_2C could be attributed by Eqs. 2 and 3 which occur in the temperature range of 1000 to 1300 °C as reported in [32], with hexagonal crystal system and P-3m1 space group.

$$\mathrm{WC} \rightarrow \mathrm{W} + \mathrm{C} \tag{2}$$

$$2W + C \rightarrow W2C \tag{3}$$

The complex ternary carbide phase of W_6Fe_6C is known for its high microhardness value [10], with cubic crystal structure and Fd-3m space group. The formation of W_6Fe_6C could be attributed to the following possible chemical reaction of Eq. 4.

$$6W + 6Fe + C \rightarrow W_6Fe_6C \tag{4}$$

With a further increase in sintering temperature, no significant difference is observed. The phases formed are similar to those reported at 1100 °C, except for the presence of traces of FeCo. The formation mechanism of equiatomic FeCo is reported in [33] and concluded that the formation takes place by an interfacial reaction between the constituents. The formation of the so-called eta carbides or M_6C, such as Co_3W_3C and Fe_3W_3C, is also evident when the temperature is raised to 1150 °C along with WC, FeO, FeCo, iron-tungsten (WFe) and cobalt iron (Co_3Fe_7). The corresponding peaks are shown in Fig. 9 and phase information is listed in Table 2. The formation of such metallic mesophases is expected to form at or above 1100 °C [34, 35].

Table 2 Phases and their crystal structure information obtained from XRD spectra

Sym	Phases	Chemical formula	Card no	Crystal system	Space group	Space group number
1000 °C						
W	Tungsten carbide	WC	04-004-6809	Hexagonal	P-6m2	187
L	Cobalt iron	Fe3Co	04-014-6028	Tetragonal	P4/mmm	123
I	Iron	Fe	00-001-1262	–	–	–
1050 °C (W and as follows)						
M	Iron manganese	FeMn	01-083-4582	Anorthic	P1	1
O	Iron oxide	FeO	04-011-7343	Cubic	Fm-3m	225
Y	Tungsten carbide	W2C	04-008-1623	Hexagonal	P-3m1	
D	Tungsten iron carbide	W6Fe6C	04-010-7470	Cubic	Fd-3m	227
1100 °C (W, M, D, O, Y and as follows)						
B	Cobalt iron	FeCo	04-014-6028	Cubic	Pm-3m	221
1150 °C (W, O, B and as follows)						
G	Cobalt tungsten carbide	Co3W3C	01-078-3750	Cubic	Fd-3m	227
T	Iron tungsten carbide	Fe3W3C	01-078-3749	Cubic	Fd-3m	227
F	Iron tungsten	WFe	04-004-2476	Cubic	Im-3m	229
N	Cobalt iron	Co3Fe7	00-048-1817	Cubic	Pm-3m	221

The formation of Co_3W_3C phase could be described as the diffusion of Co atoms into WC particles at high temperature. The possible reaction that could take place can be presented by Eq. 5. [36], with cubic crystal system and Fd-3m space group.

$$3Co + 3WC + O_2 \Leftrightarrow Co_3W_33C + 2CO \quad (5)$$

The formation of Fe_3W_3C is also clearly evident at this temperature. The possible chemical reaction that could take place is shown in Eq. 6 [37], with similar crystal structure as Co_3W_3C.

$$3Fe + 3WC \rightarrow Fe_3W_3C + 2C \quad (6)$$

The formation of these phases is important for bonding of the joining materials. They have superior mechanical properties which include higher bulk modulus [38] and microhardness [9]. Thus, the presence and amount of these phases directly influence the stability and mechanical properties of the composite material. Moreover, the formation of such phases confirms the interdiffusion of alloying elements. This indicates the occurrence of stronger bonding between the steel and ceramic materials. However, as some of these phases are brittle in nature, excessive formation of them in the bonding region may also adversely affect the bonding quality. Therefore, it is important to control the experimental conditions to maintain an accurate amount.

3.3 Physical and mechanical properties

3.3.1 Density

The mechanical properties of cemented carbides can be improved using superfine/nanoscale powders and optimising sintering techniques [39]. Owing to a simultaneous system of heating and pressurising, SPS offers the advantage of achieving high densification at lower temperature by rapid elimination of porosity and voids, and rendering fine grain structures. Figure 10 a and b show representative SEM images displaying the change of microstructure from the punch area and towards the bonding interface. It is evident that the area close to punch shows higher density. In contrast, the area far

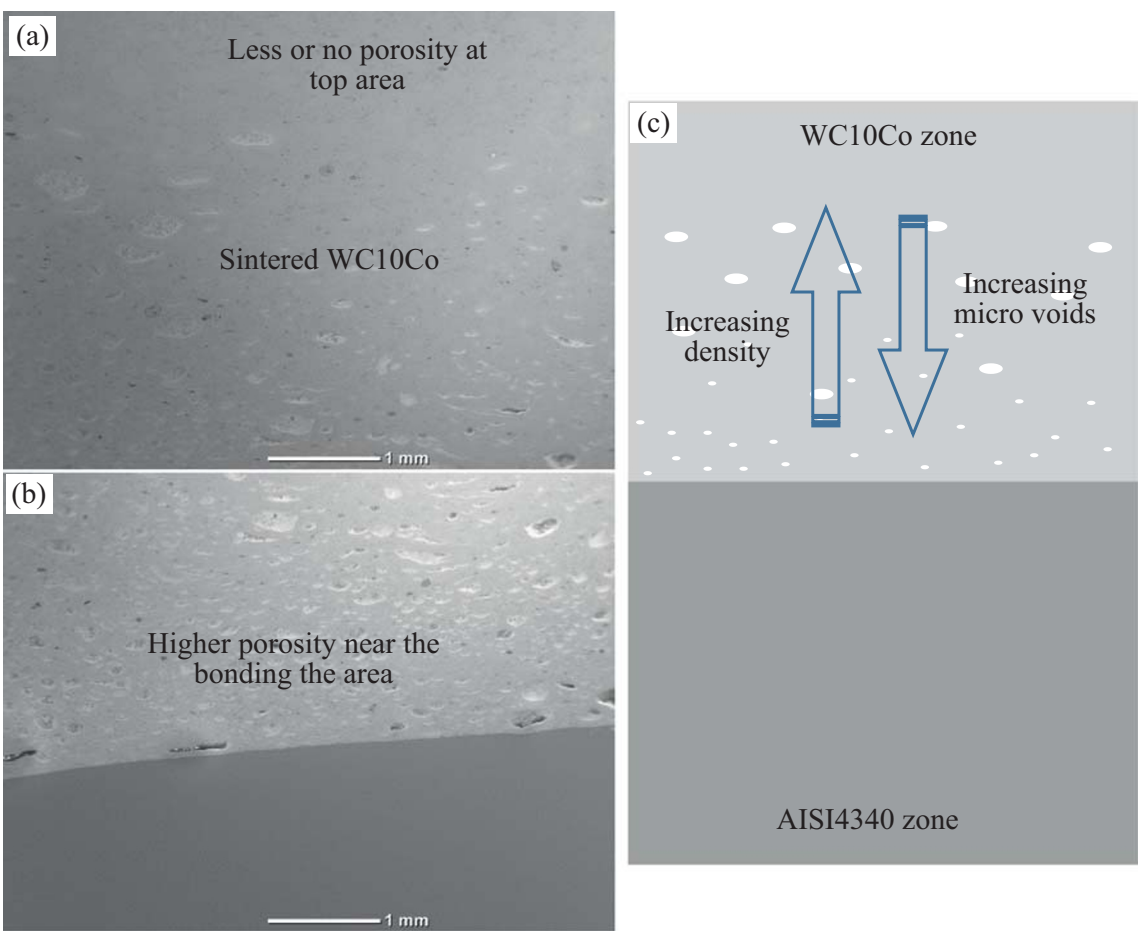

Fig. 10 Typical SEM images obtained at 1050 °C, sintered for 20 min, under 80-MPa pressure, showing the densification of **a** WC10Co, **b** decrement of density towards the bonding interface and **c** schematic diagram illustrating the phenomena of density occurred during SPS sintering

from punch and close to the bonding area shows slightly lower density. This phenomenon is explained by schematic diagram as presented in Fig. 10c. The reason for the appearance of such phenomena is discussed in Section 3. This could be eliminated by allowing more sintering time.

The results obtained for density are summarised in Fig. 11, presented with their standard deviation. It can be seen that the density was determined by measuring the weight of the used powders for each sample before the experiment and followed by dividing it with the magnitude of the volume which was measured after the sintering is completed. Three samples have been used to provide each point. It is evident that with increasing sintering temperature, the quality of sintered WC10Co increases. A continuously increasing trend of density is clearly observed with the increasing temperature. However, there is a sharp rise at 1050 °C, after that smooth increment is observed. The maximum density was achieved at a temperature of 1150 °C (99.34% compared with conventional density of WC10Co).

3.3.2 Microhardness

Figure 12 presents the influence of sintering temperature on microhardness of the WC10Co/AISI4340 bilayered composite, obtained by Vickers microhardness tester (Matsuzawa Via-F). The distance between the two successive indentations is about 100 μm. Figure 12b shows the schematics of the indentation measuring points, and the microhardness profile is presented as a function of indentation points. The indentation points from the top to bottom in Fig. 12b are presented along the *X*-axis from left to right in Fig. 12a. A clear trend of increasing hardness due to increasing sintering temperature is observed which is analogous to the results attained in density analysis. Another trend also observed is the continuous decrease of hardness towards the bonding interface. This is because of lower densification in those areas as discussed in

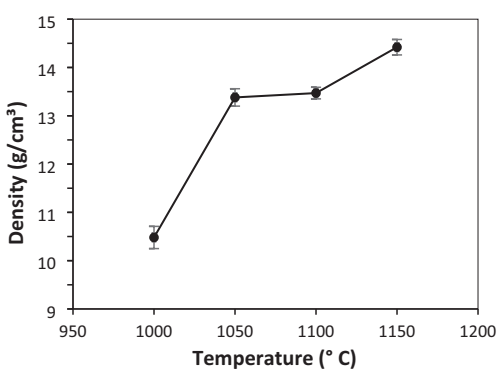

Fig. 11 Results of the density analysis obtained at different sintering temperatures

previous section. At lower temperatures, such as 1000 °C, the average hardness reported is 1280 HV. This occurs because of incomplete densification of the metal powders and the presence of bulk volume of porosity as mentioned earlier. The trendline (Fig. 12a) indicates the decreasing microhardness from the carbide region to bonding interface and then steady microhardness across the steel region. The microhardness values across the steel section are found to be similar with an average of 390 HV. No significant change is observed because of nonappearance of any visible phase change of the steel part. An increase in experimental temperatures causes continuous improvement of the hardness. The average maximum hardness was achieved at 1150 °C (1909 HV). The reason for achieving such high hardness is attributed to the use nanocrystalline powders and SPS technique. The mechanical properties, e.g. hardness, of cemented tungsten carbide using nano-sized WC–Co powders are significantly higher than what could be achieved using conventional powders [38].

3.3.3 Tensile properties

Figure 13 displays the true stress-strain curves showing the effects of varied temperatures during SPS sintering and bonding of WC10Co powders and solid AISI4340. It can be clearly observed that the bilayered composite was subjected to elastic deformation, uniform plastic deformation and a mixture of brittle and ductile fracture with the increase of strain. These phenomena are also evident from the SEM micrograph as presented in Fig. 14. As can be seen in Fig. 13, the maximum direct bonding strength is reached to ~ 183 MPa at 1150 °C. It can be seen that the stress-strain behaviour up to the strain of 0.15% is not considerable. Additionally, the behaviour is similar for all samples with the bonding strength reaching a nominal value of ~ 20 MPa. The elastic point is situated ~ 120 MPa, and then the curve goes as slightly uniform plastic deformation. It also appears that the strain is limited to ~ 0.23. This value is lower than that obtained at 1050 °C and 1100 °C, which are ~ 0.25 and 0.29 respectively. This phenomenon can be explained as the presence of increased intermetallic phases at higher temperature causes brittle fracture as also evident from the SEM micrograph shown in Fig. 14. Thus, the curve exhibits complex stress-strain characteristics where three distinct regions are clearly observed—an initial linear elastic region, a stress plateau and lastly a plastic hardening region. The reason for the appearance of such complex nature is attributed to the presence of three different regions of steel, a steel-carbide interface and carbide, in

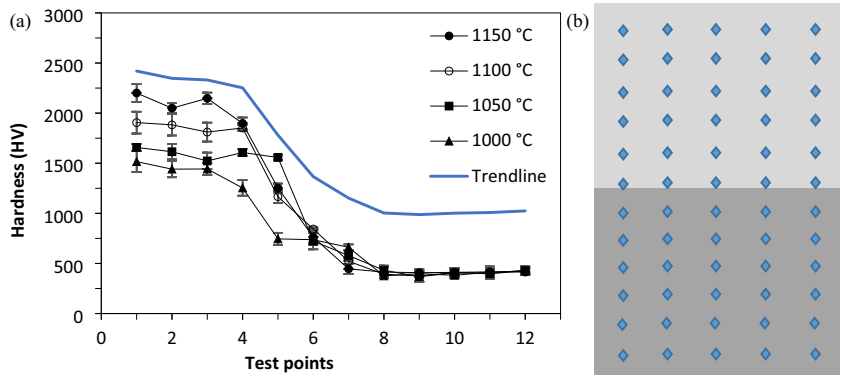

Fig. 12 **a** Microhardness profiles showing the influence of sintering temperature of the WC10Co/AISI4340 bilayered composite presented as a function of test points across the sample, and **b** schematic diagram showing measuring indentation points in each sample

the same materials. From the secondary axis, this is apparent that an increase in sintering temperatures results in increased bonding strength. From temperature 1000 to 1100 °C, the increment is somewhat in a regular pattern; however, the increment at 1150 °C is comparatively sharper. Correspondingly, the curves obtained at temperatures from 1000 to 1100 °C are of ductile nature, while the rest is of brittle nature. These values are comparable to our previous studies as reported in [26, 27, 32].

Figure 14 shows the microstructure of the fractured surfaces at WC10Co and AISI4340 bonding interfaces, obtained by miniature tensile test. At lower temperatures, the fracture occurred mostly in the carbide regions, indicating incomplete densification. In contrast, at higher temperature, the fracture occurs at the bonding interface. Hence, it is worth mentioning that, though the fracture at higher experimental temperature occurred at the bonding interface, however, from the naked eyes' observation, it was found that the breakage occurred slightly to the carbide sides. The samples at lower experimental temperatures, e.g. 1000 °C, which were broken at the bonding interface, are basically featureless. The samples which are broken at carbide regions are not shown. A typical example is presented in Fig. 14a. The grey planular island as shown on the fracture of Fig. 14a is the carbide side. When the bonding temperature increases to 1050 °C, the failure occurs in ductile nature as evident from the dimpled area shown in Fig. 14b. In addition, some transgranular brittle failures are also observed as shown in Fig. 14b. These features continue with the samples obtained at 1100 °C, with slight increase in brittle fracture. At temperatures of 1150 °C, the brittle fracture becomes dominant as evident from the cleavage planes in Fig. 14c. Figure 14d presents the fracture surface on the ceramic sides, while Fig. 14a on the other. Some Kirkendall microvoids are also developed as indicated by the arrows shown in Fig. 14d. The observed different phases as discussed earlier allow us to deduce that the failure at elevated temperature occurs due to intermetallic ternary phases, and in some places, fracture propagates in sintered carbide areas which are close to intermetallics.

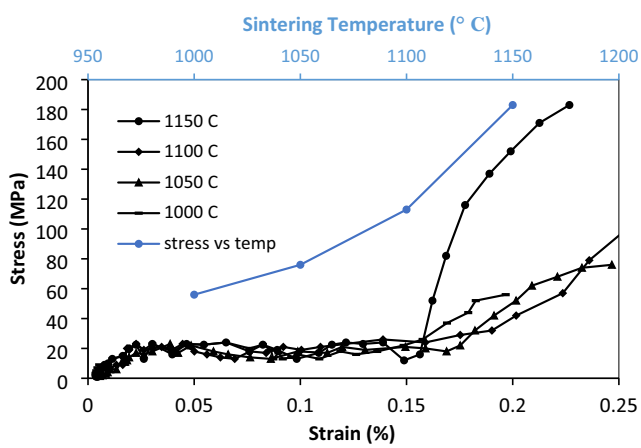

Fig. 13 True stress-strain curve obtained by miniature tensile test, showing the effects of sintering temperatures and bonding strength versus the temperature applied, during sintering and bonding of WC10Co and AISI4340

Figure 15 presents one typical micrograph of the sample sintered at 1100 °C and for 5 min, showing the elemental areal distribution at the bonding interface of WC10Co and AISI4340. Figure 16 displays the corresponding spectrum showing their composition in mass and atomic percentage on the fracture surface. In Fig. 16, the white area shows the presence of the elements. The dark area shows the unavailability of the data. This is because the EDS cannot perform the analysis deep into the valley that is created on the fracture surface during the miniature tensile test. From the elemental areal maps, it is clearly seen that the elemental diffusion occurred on the bonding interface. This also gives evidence that the fracture that occurred in the bonding interface is slightly close to the carbide side.

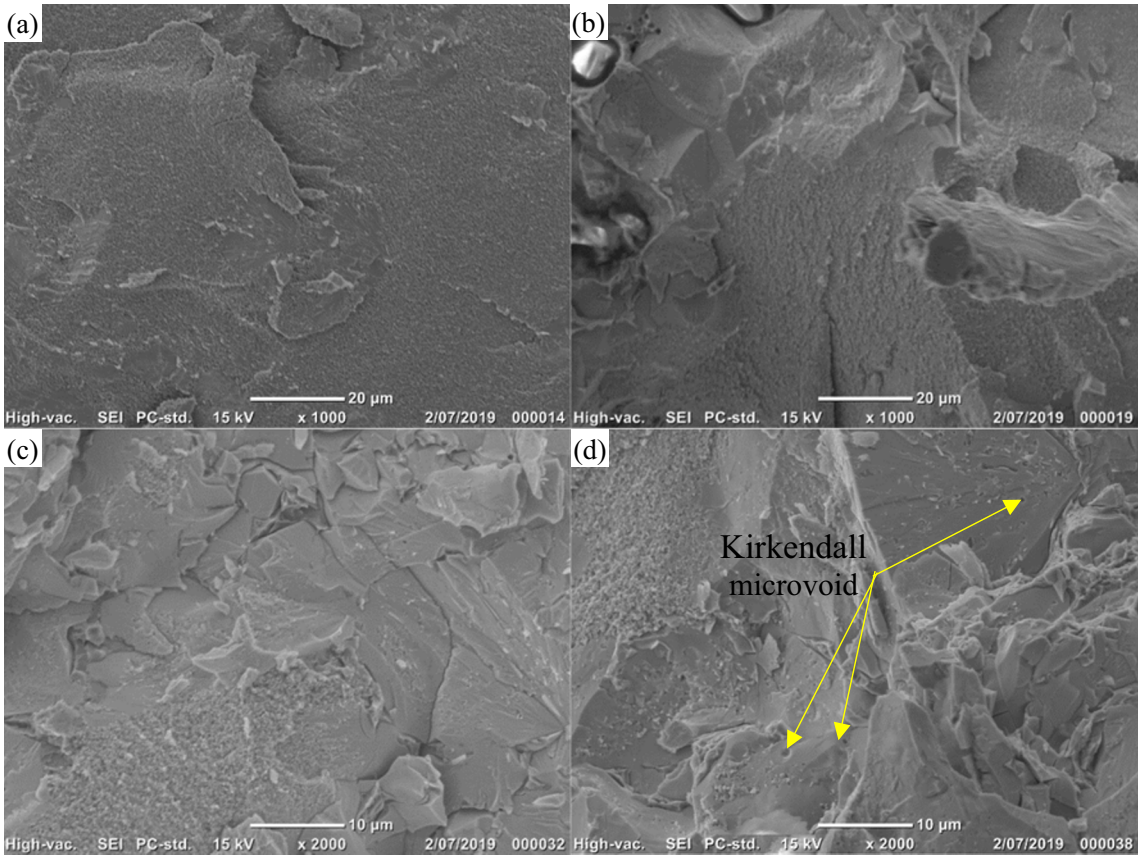

Fig. 14 Microstructure of the fracture surfaces of the joints sintered for 5 min and bonded at **a** 1000 °C, **b** 1050 °C, **c** 1150 °C, steel side and **d** 1150 °C, ceramic side

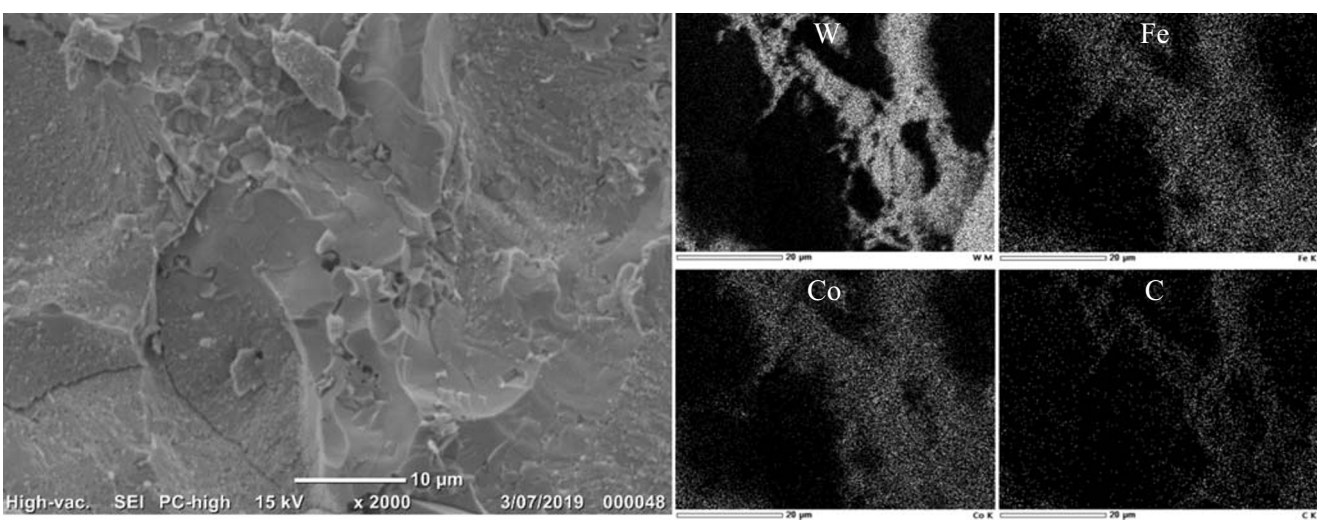

Fig. 15 SEM micrograph of the sample obtained at 1100 °C and sintered for 5 min, and elemental areal map showing the key elements e.g. W, Fe, Co and C elements

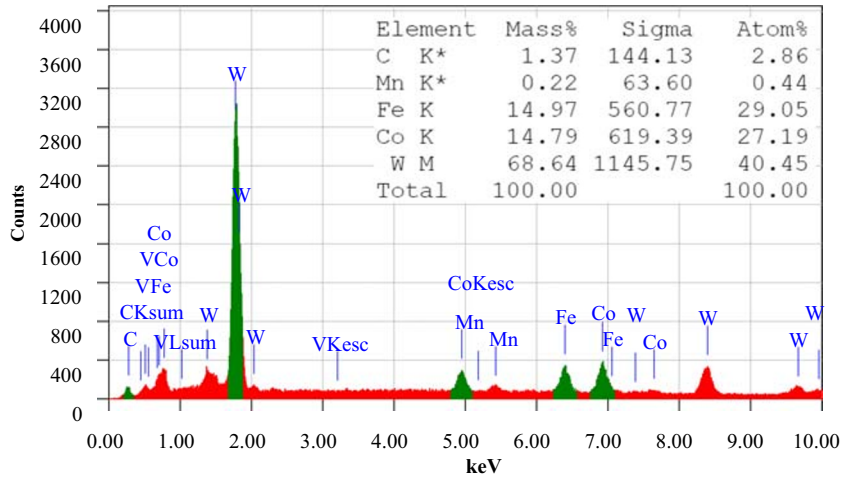

Fig. 16 Typical example of the elemental spectrum for the sample as mentioned in Fig. 15 showing the peaks of the elements and their compositions in mass and atomic percentages

4 Conclusions

SPS exhibits a potential technique for bonding dissimilar carbide and steel materials, i.e. WC10Co and AISI4340. Successful experiments were conducted followed by microstructural analysis and mechanical property evaluation. No significant fracture or delamination was observed at the bonding interface. Nevertheless, the quality of bonding improved with increasing temperature. From microstructural observations, a continuous, crack-free bond confirms sound metallurgical bonding between WC10Co and AISI4340 materials. The results obtained could be compared with our previously developed method called Hot Compaction Diffusion Bonding (HCDB) in terms of sintering the carbide powders and attainment of their improved mechanical properties; however, in SPS, no significant reaction layer was observed. This is probably because of insufficient sintering time which was limited to 5 min during sintering in SPS. This also led to the limited formation of ternary intermetallic carbides at the bonding interface. SPS provided excellent mechanical properties at a comparatively lower temperature in a short period of sintering time. The average maximum hardness was achieved at 1150 °C (1909 HV). The reason for achieving such high hardness is attributed to the use nanocrystalline powder and SPS technique. The maximum density achieved at a temperature of 1150 °C is 99.34% compared with that of the conventional one. The maximum tensile strength of the bond reached ~ 183 MPa at 1150 °C. However, the elastic point is situated at ~ 120 MPa, and then the curve goes as slightly uniform plastic deformation. The tensile strength obtained in SPS is found significantly higher than that of the reported result in previous studies. To the best knowledge of the authors, there is no literature where SPS is used for joining WC10Co and AISI4340, so it is expected that this study can provide an important future reference in order to manufacture dissimilar bilayered composite materials. Such bilayered composite also possesses significant industrial application potentials where high hardness and high strength are simultaneously required in a single component.

Acknowledgements We acknowledge the use of facilities within the UOW Electron Microscopy Centre.

Funding The authors would like to thank the Australian Research Council (ARC) for its financial support for the study.

References

1. Eriksson M, Radwan M, Shen Z (2013) Spark plasma sintering of WC, cemented carbide and functional graded materials. Int J Refract Met Hard Mater 36:31–37
2. Cha SI, Hong SH, Kim BK (2003) Spark plasma sintering behavior of nanocrystalline WC–10Co cemented carbide powders. Mater Sci Eng A 351(1–2):31–38
3. Sivaprahasam D, Chandrasekar S, Sundaresan R (2007) Microstructure and mechanical properties of nanocrystalline WC–12Co consolidated by spark plasma sintering. Int J Refract Met Hard Mater 25(2):144–152
4. Huang S et al (2008) Tailored sintering of VC-doped WC–Co cemented carbides by pulsed electric current sintering. Int J Refract Met Hard Mater 26(3):256–262
5. Liu X, Song X, Zhang J, Zhao S (2008) Temperature distribution and neck formation of WC–Co combined particles during spark plasma sintering. Mater Sci Eng A 488(1):1–7
6. Liu W, Song X, Zhang J, Yin F, Zhang G (2008) A novel route to prepare ultrafine-grained WC–Co cemented carbides. J Alloys Compd 458(1):366–371

7. Hasan M, Zhao J, Jiang Z (2017) A review of modern advancements in micro drilling techniques. J Manuf Process 29:343–375
8. Hasan M, Zhao J, Jia F, Wu H, Ahmad F, Huang Z, Wei D, Ma L, Jiang Z (2020) Optimisation of sintering parameters for bonding nanocrystalline cemented tungsten carbide powder and solid high strength steel. Composite Interfaces 8:1–6
9. Hasan M, Zhao J, Jiang Z (2019) Micromanufacturing of composite materials: a review. International Journal of Extreme Manufacturing 1(1):012004
10. Zafar S, Sharma AK (2014) Development and characterisations of WC–12Co microwave clad. Mater Charact 96:241–248
11. Feng K, Chen H, Xiong J, Guo Z (2013) Investigation on diffusion bonding of functionally graded WC–Co/Ni composite and stainless steel. Mater Des 46:622–626
12. Thomazic A, Pascal C, Chaix JM. Fabrication of (cemented carbides/steel) bilayered materials by powder metallurgy. In Materials Science Forum 2010 (Vol. 631, pp. 239–244). Trans Tech Publications Ltd
13. Pascal C et al (2009) Design of multimaterial processed by powder metallurgy: processing of a (steel/cemented carbides) bilayer material. Int J Mater Prod Technol 209(3):1254–1261
14. Lee W-B, Kwon B-D, Jung S-B (2006) Effects of Cr3C2 on the microstructure and mechanical properties of the brazed joints between WC–Co and carbon steel. Int J Refract Met Hard Mater 24(3):215–221
15. Bao J, Newkirk JW, Bao S (2004) Wear-resistant WC composite hard coatings by brazing. J Mater Eng Perform 13(4):385–388
16. Zhang XZ, Liu GW, Tao JN, Shao HC, Fu H, Pan TZ, Qiao GJ (2017) Vacuum brazing of WC-8Co cemented carbides to carbon steel using pure Cu and Ag-28Cu as filler metal. J Mater Eng Perform 26(2):488–494
17. Giménez S, Huang SG, van der Biest O, Vleugels J (2007) Chemical reactivity of PVD-coated WC–Co tools with steel. Appl Surf Sci 253(7):3547–3556
18. Zhong Z, Hinoki T, Nozawa T, Park YH, Kohyama A (2010) Microstructure and mechanical properties of diffusion bonded joints between tungsten and F82H steel using a titanium interlayer. J Alloys Compd 489(2):545–551
19. Barrena M, De Salazar JG, Matesanz L (2010) Interfacial microstructure and mechanical strength of WC–Co/90MnCrV8 cold work tool steel diffusion bonded joint with cu/Ni electroplated interlayer. Mater Des 31(7):3389–3394
20. Haghshenas MS, Parvin N, Amirnasiri A (2018) Effect of bonding temperature on microstructure and mechanical properties of WC–Co/steel diffusion brazed joint. Trans Indian Inst Metals 71(3):649–658
21. Nascimento MP, Souza RC, Miguel IM, Pigatin WL, Voorwald HJC (2001) Effects of tungsten carbide thermal spray coating by HP/HVOF and hard chromium electroplating on AISI 4340 high strength steel. Surf Coat Technol 138(2–3):113–124
22. Monticelli C, Frignani A, Zucchi F (2004) Investigation on the corrosion process of carbon steel coated by HVOF WC/Co cermets in neutral solution. Corros Sci 46(5):1225–1237
23. Singh H, Goyal K, Goyal DK (2017) Experimental investigations on slurry erosion behaviour of HVOF and HVOLF sprayed coatings on hydraulic turbine steel. Trans Indian Inst Metals 70(6):1585–1592
24. Maiti AK, Mukhopadhyay N, Raman R (2009) Improving the wear behavior of WC-CoCr-based HVOF coating by surface grinding. J Mater Eng Perform 18(8):1060–1066
25. Toparli M, Sen F, Culha O, Celik E (2007) Thermal stress analysis of HVOF sprayed WC–Co/NiAl multilayer coatings on stainless steel substrate using finite element methods. J Mater Process Technol 190(1–3):26–32
26. Hasan M, Zhao J, Huang Z, Wu H, Jia F, Jiang Z (2019) Effects of holding time on the sintering of cemented tungsten carbide powder and bonding with high-strength steel wire. J Mater Eng Perform 28(7):4074–4085
27. Hasan M, Zhao J, Huang Z, Wei D, Jiang Z (2019) Analysis and characterisation of WC-10Co and AISI 4340 steel bimetal composite produced by powder–solid diffusion bonding. Int J Adv Manuf Technol 103(9):3247–3263
28. Luo L et al (2015) An experimental and numerical study of micro deep drawing of SUS304 circular cups. Manuf Rev 2(27):1–7
29. Asano H, Bando Y, Nakanishi N, Kachi S (1967) Order-disorder transformation of Fe–Co alloys in fine particles. Trans Jpn Inst Metals 8(3):180–184
30. Persson K (2016) Materials Data on Fe3Co (SG:123) by Materials Project. LBNL Materials Project; Lawrence Berkeley National Lab. (LBNL), Berkeley, CA (United States): United States
31. McCammon C, Ringwood A, Jackson I (1983) Thermodynamics of the system Fe—FeO—MgO at high pressure and temperature and a model for formation of the Earth's core. Geophys J Int 72(3):577–595
32. Hasan M, Zhao J, Huang Z, Chang L, Zhou H, Jiang Z (2018) Analysis of sintering and bonding of ultrafine WC powder and stainless steel by hot compaction diffusion bonding. Fusion Eng Des 133:39–50
33. Collins GS, Meeves BH (1993) Formation of FeCo by mechanical alloying. Scripta metallurgica et materialia 29(10)
34. Suetin DV, Shein IR, Ivanovskii AL (2009) Structural, electronic and magnetic properties of η carbides (Fe3W3C, Fe6W6C, Co3W3C and Co6W6C) from first principles calculations. Phys B Condens Matter 404(20):3544–3549
35. Machado IF, Girardini L, Lonardelli I, Molinari A (2009) The study of ternary carbides formation during SPS consolidation process in the WC–Co–steel system. Int J Refract Met Hard Mater 27(5):883–891
36. Guilemany JM, de Paco JM, Miguel JR, Nutting J (1999) Characterization of the W2C phase formed during the high velocity oxygen fuel spraying of a WC + 12 pct Co powder. Metall Mater Trans A 30(8):1913–1921
37. Telmenbayar L, Temuujin J (2016) Preparation of tungsten carbide from mixtures of natural wolframite and carbon-containing solid fuels with assistance of mechanical activation. J Ceram Process Res 17(5):489–493
38. Fang ZZ, Wang X, Ryu T, Hwang KS, Sohn HY (2009) Synthesis, sintering, and mechanical properties of nanocrystalline cemented tungsten carbide–a review. Int J Refract Met Hard Mater 27(2):288–299
39. Goren-Muginstein G, Berger S, Rosen A (1998) Sintering study of nanocrystalline tungsten carbide powders. Nanostruct Mater 10(5):795–804

Publisher's note Springer Nature remains neutral with regard to jurisdictional claims in published maps and institutional affiliations.